

# Correlation of Microstructure to Creep Response of Hot Isostatically Pressed and Aged Electron Beam Melted Inconel 718



BENJAMIN SHASSERE, DUNCAN GREELEY, ALFRED OKELLO, MICHAEL KIRKA, PEEYUSH NANDWANA, and RYAN DEHOFF

Creep rupture samples were fabricated by additive manufacturing (AM) *via* electron beam melting (EBM) to study the effects of grain morphology (equiaxed/columnar grains) and loading direction (longitudinal/transverse) with respect to build direction on creep deformation at 923 K (650 °C) with applied stresses of 580 and 600 MPa. The observed minimum creep rates and creep rupture lives of EBM Inconel 718 after post-processing by hot isostatic pressing (HIP) were found to be comparable to wrought material. The material with equiaxed grains exhibited low creep strain (2 pct) and short creep lifetimes (800 hours), whereas longer times (approximately 4500 hours) and high creep strain (up to 23 pct) were observed for material with columnar grains. The high stress exponent ( $n > 14$ ) reflected the resistance to dislocation motion by  $\gamma''$  particles during creep. A precipitate-free zone (PFZ) was observed around the grain boundary  $\delta$  phase. Creep damage occurred as voids and cracks in the PFZ. Optimal post-processing of EBM Inconel 718 material should be explored to prevent  $\delta$  phase embrittlement.

<https://doi.org/10.1007/s11661-018-4812-z>

© The Minerals, Metals & Materials Society and ASM International 2018

## I. INTRODUCTION

TEMPERATURES can often exceed 1073 K (800 °C) in the gas turbine engines of airplanes and power generation plants.<sup>[1]</sup> High temperature-resistant alloys are required in these extreme environments. Nickel-based superalloys are often utilized due to their favorable high-temperature creep strength, corrosion and oxidation

resistance, and good weldability.<sup>[2,3]</sup> Inconel 718 is one such Ni-Fe-based superalloy commonly used in these applications. The alloy derives its high-temperature creep performance from precipitation of  $\gamma'$  ( $\text{Ni}_3\text{Al}$ ) and  $\gamma''$  ( $\text{Ni}_3\text{Nb}$ ) particles in an FCC- $\gamma$  matrix.<sup>[2,4,5]</sup> The microstructure also includes grain boundary  $\delta$  precipitates and MC-type carbides that provide additional strengthening.<sup>[6–9]</sup>

To date, Inconel 718 has been produced in both wrought and cast forms. More recently, opportunities for freedom of design and near-net shape production have driven research in additive manufacturing (AM) techniques for this alloy. Electron beam melting (EBM), selective laser melting (SLM), and laser engineering net shaping (LENS) are a few such AM techniques that use a heat source for melting metal powder and building the final component layer by layer.<sup>[10–13]</sup> However, the correlation of the unique microstructures to mechanistic properties for AM builds is not yet fully understood. To attain high-temperature creep performance of conventional Inconel 718, microstructure is controlled by the application of traditional processing methods. The creep performance of AM builds of EBM has yet to be correlated to the microstructures, which are attributable to process variables including build direction, complex thermal conditions (solidification rates, thermal gradients, *etc.*), and designed melt strategies.

---

BENJAMIN SHASSERE is with the Materials Science and Technology Division, Oak Ridge National Laboratory, Oak Ridge, TN 37831. Contact e-mail: shassereba@ornl.gov DUNCAN GREELEY and ALFRED OKELLO are with the Manufacturing Demonstration Facility, Oak Ridge National Laboratory, Knoxville, TN 37932. MICHAEL KIRKA, PEEYUSH NANDWANA, and RYAN DEHOFF are with the Materials Science and Technology Division, Oak Ridge National Laboratory and also with the Manufacturing Demonstration Facility, Oak Ridge National Laboratory.

This manuscript has been authored [or, co-authored] by UT-Battelle, LLC, under Contract DE-AC05-00OR22725 with the US Department of Energy (DOE). The US government retains and the publisher, by accepting the article for publication, acknowledges that the US government retains a nonexclusive, paid-up, irrevocable, worldwide license to publish or reproduce the published form of this manuscript, or allow others to do so, for US government purposes. DOE will provide public access to these results of federally sponsored research in accordance with the DOE Public Access Plan (<http://energy.gov/downloads/doe-public-access-plan>).

Manuscript submitted December 8, 2017.

Article published online July 16, 2018

Previous studies have characterized the microstructure of AM Inconel 718 and the associated mechanical properties. In the as-built condition using traditional AM melt patterns with laser additive manufacturing and EBM, spatial heterogeneity in the microstructure was found to be a function of layer height.<sup>[13,14]</sup> The microstructural heterogeneity in EBM builds could be largely homogenized with post-processing such as hot isostatic pressing (HIP) and solution treatment and aging (STA).<sup>[15]</sup> After post-processing, the anisotropic room temperature tensile properties associated with EBM in the longitudinal orientation (parallel to the build direction) showed tensile properties comparable to wrought products.<sup>[15]</sup> However, such studies have not reported the relationships of processing conditions or differences in melt strategies to the creep performance of 718.

Recently, AM process parameters have been manipulated to control the microstructure of builds to influence the mechanical properties. Kirka *et al.*,<sup>[16]</sup> successfully controlled the texture of EBM Inconel 718 builds, which gave either columnar or equiaxed grains by utilizing standard melt fill or point net melt strategy, respectively. Anisotropic tensile properties were obtained for the columnar microstructures, and isotropic tensile properties resulted from the equiaxed microstructures at room temperature. The room temperature tensile and fatigue properties of the equiaxed microstructure were comparable to wrought Inconel 718.<sup>[16]</sup> However, the effect of microstructural anisotropy and texture on the creep properties of EBM Inconel 718 have not yet been evaluated. Therefore, the objective of this study is to characterize the creep behavior of EBM Inconel 718 and correlate behavior to the columnar or equiaxed microstructures. Creep testing at 923 K (650 °C) of Inconel 718 was performed on specimens with columnar or equiaxed microstructures in the longitudinal and transverse orientations.

## II. EXPERIMENTAL APPROACH

Plasma-atomized powder of Inconel 718, manufactured by Advanced Powders and Coatings (Quebec, Canada), was used for the electron beam melting process. The powder had a size distribution of 40 to 120  $\mu\text{m}$  and a nominal composition given in Table I.

### A. Experimental Setup

An Arcam S12 EBM machine running EBM Control V4.1.89 was used for the builds. A 304-stainless steel (150 mm  $\times$  150 mm  $\times$  10 mm) start-plate was used. A powder bed temperature of 1373 K (1100 °C) was

attained and held for 30 minutes to sinter the powder beneath the start-plate to provide stability. A chamber vacuum level of  $2 \times 10^{-3}$  mbar was maintained, and the gun accelerating voltage set to 60 kV during the build process. A constant layer thickness of 50  $\mu\text{m}$  was used.

Two melt strategies were used to distinguish the bulk-scale mechanical properties of the two textures produced by the Arcam EBM process. Description of the melt strategies is detailed elsewhere.<sup>[16]</sup> The build layout is shown in Figure 1, adapted from Ref. 16. The layout was composed of square columns (colored) (15 mm  $\times$  15 mm  $\times$  100 mm) and rectangular columns (gray) (100 mm  $\times$  15 mm  $\times$  100 mm). The square columns were used to test longitudinal direction and the rectangular columns were used to test transverse direction. The parts were evenly split between the two melt strategies. A few of the square columns were used for tensile testing and microstructure characterization before and after post-processing; details are described elsewhere.<sup>[16]</sup>

### B. Material Post-Processing

After the build was completed, the columns were subjected to a two-stage post-processing treatment composed of HIP and STA. First, HIP was performed using a Quintus QIH-9 with heating and cooling rates up to 315 K (42 °C) per minute. HIPing took place at a temperature of 1473 K (1200 °C) and a pressure of 120 MPa for a total time of 240 minutes. Subsequently, STA was conducted in a vacuum furnace programmed for the following conditions: hold at 1339 K (1066 °C) for 60 minutes, followed by a double aging cycle at 1033 K (760 °C) for 10 hours, and 923 K (650 °C) for 10 hours.<sup>[17]</sup>

### C. Creep Rupture Testing

Creep testing was performed following ASTM standard E139.<sup>[18]</sup> Testing was performed at Joliet Metallurgical (Joliet, IL, USA) and Oak Ridge National Laboratory (ORNL) (Oak Ridge, TN, USA) at stress levels of 580 and 600 MPa, respectively. The creep testing at Joliet Metallurgical was performed on a Satec lever arm 16:1 ratio constant load creep frame, and the strain was measured by dial gages. The creep testing at ORNL was performed on a custom 16:1 lever arm ratio with a linear variable differential transducer (LVDT) sensor for measuring strain. The test temperature was held at a constant 923 K (650 °C) for all samples, and was achieved using three-zone resistance heating furnaces attached to the creep machines. All tests were performed in lab air. The temperatures were monitored throughout by two K-type thermocouples directly attached to the gage section.

### D. Microstructure Characterization

After creep testing, the samples were sectioned using a low-speed diamond saw and mounted longitudinally in phenolic resin. The mounted samples were prepared using standard metallographic techniques. A final polish was

**Table I. Nominal Chemical Composition of the Inconel 718 Powder in Weight Percent**

Ni	Cr	Fe	Nb	Mo	Ti	Cu	Al	C
Balance	18.5	18.5	5	3	1	0.15	0.5	0.05

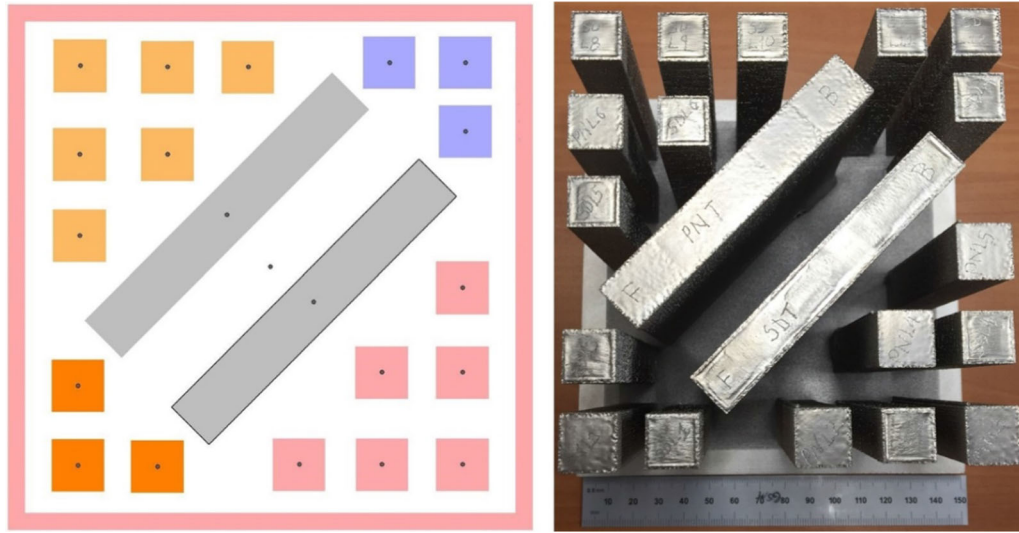


Fig. 1—A CAD model showing the square and rectangular columns (left). The finished build is shown on the right. Adapted from Ref. [16].

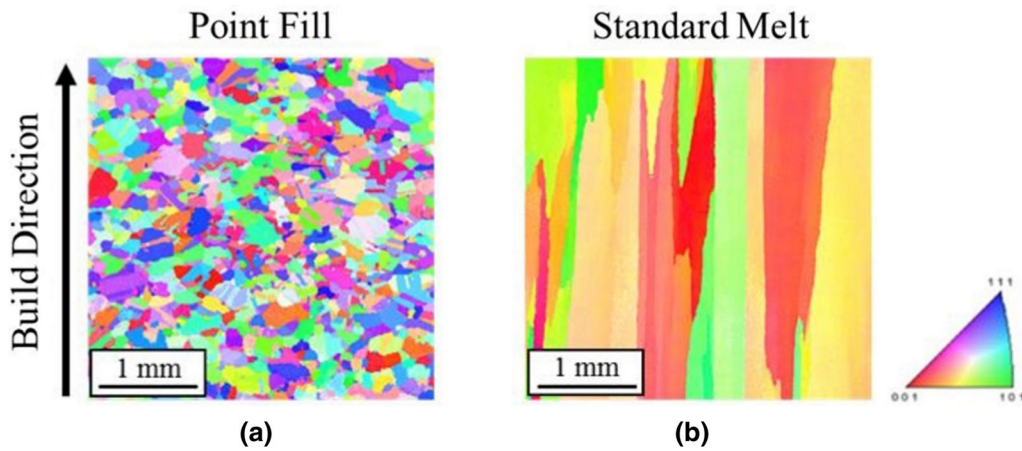


Fig. 2—Grain orientation maps showing grain structure after post-processing in point fill (equiaxed) (a) and standard melt fill (columnar) (b) of EBM Inconel 718 builds.

achieved using  $0.05 \mu\text{m}$  colloidal silica on a Buehler Vibromet II® for more than 6 hours. The samples were then etched by swabbing with glycerregia. Microstructure imaging was conducted using scanning electron microscopy (SEM) on a JEOL 6500 FEG-SEM at 20 kV equipped with EDAX electron back scatter diffraction (EBSD). Fracture surfaces of the creep rupture specimens were imaged using a Hitachi-3400N SEM at 15 kV.

### III. RESULTS AND DISCUSSION

#### A. Pre-creep Microstructure

Electron backscatter diffraction was used to characterize the two different grain structures produced from the point net fill strategy (equiaxed) and standard melt fill strategy (columnar). The representative grain orientation maps of the microstructures are shown in Figure 2.

The grain size, after post-processing, in the builds with equiaxed grains were 270 to  $310 \mu\text{m}$ . The columnar

grain width, after post-processing, varied between 200 and  $500 \mu\text{m}$ . The microstructures of builds prior to creep testing, are shown in Figure 3. The microstructures consisted of the  $\gamma$  matrix with  $\gamma'/\gamma''$  precipitates in both the equiaxed and columnar grained builds. The build with an equiaxed grain structure showed only a few carbides in the matrix or on grain boundaries, but grain boundary  $\delta$  precipitates were present. Grain boundary carbides and  $\delta$  phase were present in the columnar grain builds.

#### B. Creep Response of Inconel 718 at 923 K (650 °C)

The corresponding creep strain versus time curves are shown in Figure 4. Creep strain rates were obtained from the steady-state regime. The details of the creep behavior are listed in Table II. Note that the equiaxed transverse sample stressed at 580 MPa failed prematurely, due to possible deposition defects. The two curves for the columnar longitudinal samples stressed at

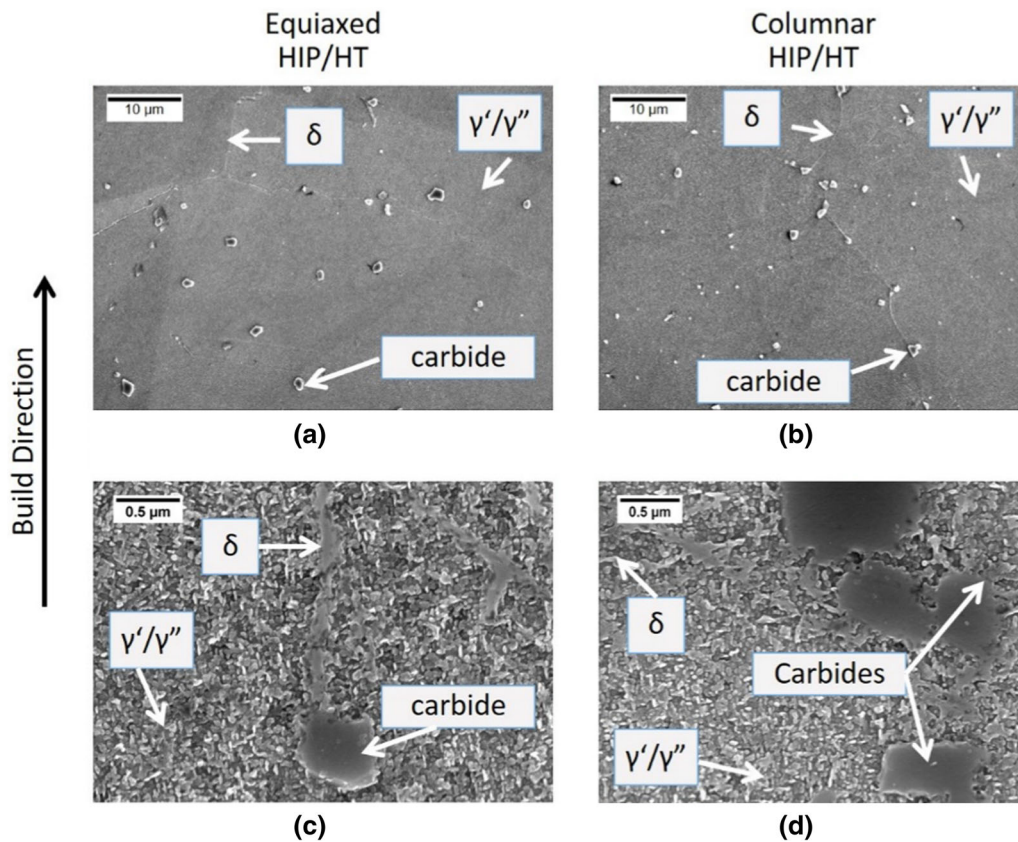


Fig. 3—SEM images showing microstructure of post-processed EBM Inconel 718 prior to creep testing. (a) and (b) are low magnification images. (c) and (d) are high-magnification images.

580 and 600 MPa both showed traditional creep strain curves; a short primary stage, a dominant steady-state regime, and tertiary regime lasting longer than 1000 hours. The 580 MPa sample does show a shorter creep life. This goes against intuition, but this is due to experimental creep life spread. Experimental spread is widely observed and is seen in Figure 5 as the solid parallel lines. The remaining samples showed a dominant steady-state regime, but had a short tertiary regime (< 400 hours stressed at 580 MPa, and < 100 hours stressed at 600 MPa). The dominant steady-state creep regime and time to failure for all but the single anomalous sample were consistent with wrought 718 at 923 K (650 °C).<sup>[19,20]</sup>

It is evident from the curves of EBM Inconel 718 that the columnar grain structure has better creep performance than the equiaxed grain structure. Most modern Ni-based alloys show creep deformation behavior that is dependent on grain structure. VerSnyder and Guard<sup>[21]</sup> demonstrated that improved creep rupture strength and reduced scatter in mechanical properties could be achieved with directional solidification (DS) compared to conventionally cast (CC) superalloys. Other studies have shown creep damage and cracks preferentially initiating on grain boundaries perpendicular to the loading direction.<sup>[22,23]</sup> The improvement in creep rupture strength in columnar-grained Inconel 718 builds can be attributed to the reduction of the area of transverse grain

boundaries.<sup>[24]</sup> The EBM Inconel 718 builds with equiaxed grain structures showed an average rupture strain of 1.75 pct for the two loading conditions. The builds with a columnar microstructure had an average rupture strain of 4.2 pct, when loaded in the transverse direction. However, the builds with a columnar microstructure loaded in the longitudinal direction had rupture strains between 18 and 23 pct. This shows the importance of grain structures in creep deformation of Inconel 718. The equiaxed microstructures exhibited rupture strains lower than the wrought material.<sup>[25,26]</sup> The EBM columnar builds loaded in the longitudinal direction exhibited rupture strains 1.5 times higher than the wrought and 5 times higher than the EBM equiaxed counterparts. This shows the strong dependence of the creep rupture strength on the grain structures.

The creep life of EBM Inconel 718 compares well with the data on wrought 718, and this is represented in Figure 5.<sup>[25–27]</sup> The wrought 718 has a scatter band spanning 2 orders of magnitude for creep life (100 to 10000 hours) at 580 to 600 MPa. The creep life of EBM Inconel 718 with equiaxed microstructures is within the midrange of the spread (600 to 1100 hours). However, the longitudinally loaded samples with columnar microstructures approach 5000 hours. The observation of high ductility and creep strength for the columnar longitudinally loaded builds is consistent with the expected creep strength for directionally solidified materials compared to polycrystalline material.

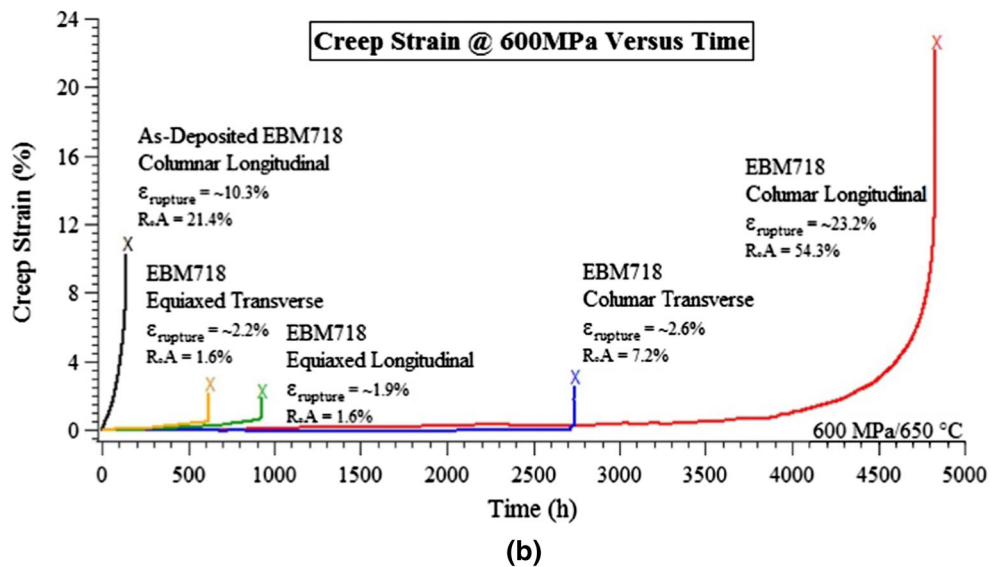
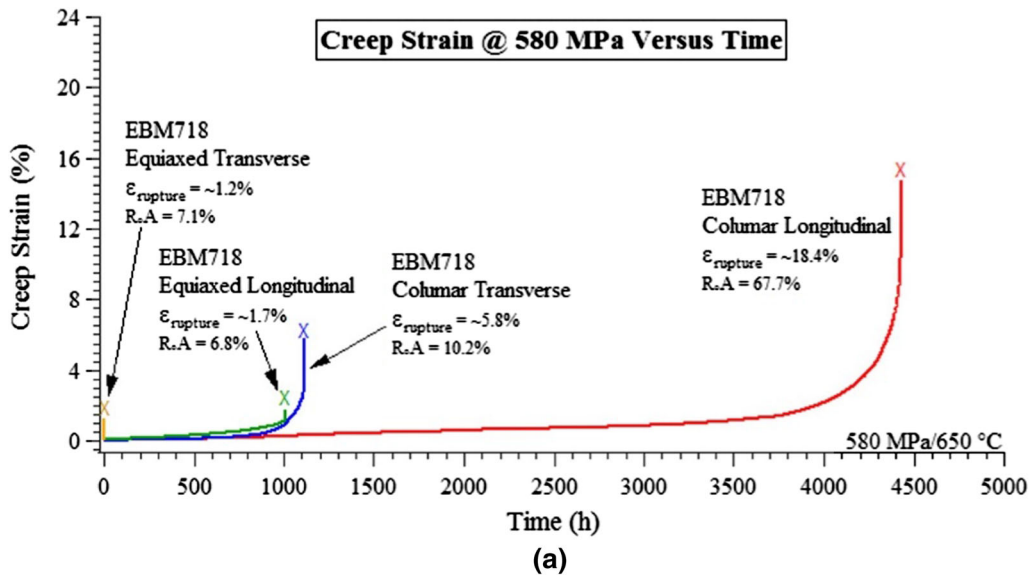


Fig. 4—Creep strain-time curves at 923 K (650 °C) and 580 MPa (a) and 600 MPa (b). Note that the equiaxed material loaded transverse to the build direction failed prematurely.

It is prudent to compare the results in this study with work from other authors where additive manufacturing was utilized. In this work, the observed creep lifetimes for the post-processed builds are superior to other as-deposited AM Inconel 718 builds. Kuo *et al.*<sup>[28]</sup> observed inferior creep life of direct metal laser sintering (DMLS) builds when compared to wrought materials, with as-deposited and STA post-processed builds having creep lives less than 300 hours at 923 K (650 °C) at 550 MPa. The authors found that the poor creep properties were due to weak transverse grain boundaries, especially the interdendritic boundaries.

### C. Post-creep Microstructure

Figures 6 and 7 show the microstructures of EBM Inconel 718 after creep rupture at 923 K (650 °C).

Figure 6 shows the microstructure of the point net melt fill strategy or equiaxed grain structure. The matrix consists of  $\gamma$  with  $\gamma'/\gamma''$  precipitates away from the grain boundaries. Carbides (1 to 2  $\mu\text{m}$ ) are observed in the matrix. The grain boundaries mainly contain  $\delta$  phase precipitates along with a few carbides at triple points. Figure 7 shows the microstructures of the standard melt fill strategy or columnar grain structure. Similar to Figure 6, the matrix again consists of  $\gamma$  with  $\gamma'/\gamma''$  precipitates away from the grain boundaries. Here the grain boundaries contain  $\delta$  phase precipitates. However, more grain boundary carbides are observed in this build, but not in meaningful quantities. In all the builds, a denuded or precipitate-free zone (PFZ), with a size of roughly between 50 and 100 nm, is observed along the grain boundary  $\delta$  phase. Given the time spent during creep (600 to 5000 hours) at 923 K (650 °C), the

**Table II. Creep Conditions and Results at 923 K (650 °C). Creep Behavior of EBM Inconel 718 at 923 K (650 °C) in Lab Air at 580 and 600 MPa. The Orientations Used Are Longitudinal (L) and Transverse (T) to the Build Direction**

Specimen	Material Condition	Orientation	Stress (MPa)	Min. Creep Rate ( $\text{h}^{-1}$ )	Min. Creep Rate (IN 718) ( $\text{h}^{-1}$ ) <sup>15</sup>	Creep Rupture Time (h)	Average Rupture Time (IN 718) (h) <sup>15</sup>	Elong. (Percent)	RA (Percent)	Elong. (IN 718) (Percent) <sup>15</sup>	RA (IN 718) (Percent) <sup>15</sup>
Columnar Equiaxed	As Built	L	600	2.00E-04	2.7 E-6 to 5.0 E-6	140	$t_{600\text{h}} = 741$	10.3	21.4	13.4 (at 620 MPa)	13.4 (at 620 MPa)
Columnar Equiaxed	Post-processed	T	600	4.40E-06	E-6	2736		2.6	7.2	MPa)	MPa)
Columnar Equiaxed		T	600	2.80E-06		620		2.2	1.6	Korth <sup>15</sup>	Korth <sup>15</sup>
Columnar Equiaxed		L	600	1.10E-06		4831		23.2	54.3		
Columnar Equiaxed		L	600	1.90E-06		922		1.9	1.6		
Columnar Equiaxed		T	580	9.80E-07	1.3 E-6 to 7.4 E-6	1110	$t_{580\text{h}} = 1055$	5.8	10.2	16.1 (at 579 MPa)	42.0 (at 579 MPa)
Columnar Equiaxed		T	580	Failed at start of test	E-6	8		1.2	7.1	Korth <sup>15</sup>	Korth <sup>15</sup>
Columnar Equiaxed		L	580	8.20E-07		4434		18.4	67.7		
Columnar Equiaxed		L	580	2.00E-06		1007		1.7	6.8		

strengthening  $\gamma''$  phase could dissociate into the  $\delta$  phase to create a PFZ.<sup>[7,29]</sup> The formation of a PFZ is a well-known phenomenon and has been observed by others.<sup>[7,29,30]</sup> In Figures 6(e) and 7(e), high-magnification images highlight the general appearance of the PFZ observed in all specimens. Creep voids and cracking are observed along the  $\delta/\gamma$  matrix interface and within the PFZ. The voids and cracks are observed along grain boundaries oriented approximately perpendicular to the loading direction in all equiaxed samples and in the transverse columnar samples. Voids were only observed along grain boundaries parallel to the loading direction in the longitudinal columnar samples.

#### D. Post-Creep Fractography

Figures 8 and 9 show the fracture surfaces of the creep rupture samples stressed at 580 and 600 MPa for the equiaxed and columnar grain structures loaded in the longitudinal and transverse directions. The samples with equiaxed grain structure, in Figure 8, show grain facets. The facets indicate intergranular cracking, confirming the grain boundary separation seen earlier in Figure 6. Upon close inspection, the surfaces of the facets, or grain boundaries, reveal the presence of voids with particles at the bottom (see Figures 8(e) and 9(e)). Rapid void linkage along transverse intergranular boundaries appears to cause cracking and failure. These micro-level mechanisms are associated with the brittle attributes of the fracture: faceted surface, low creep strain to failure, the absence of necking, and low reduction of cross-sectional area. The rapid failure is evident in the creep curves, with the tertiary regime lasting less than 400 hours.

Figure 9 shows the fracture surface of the samples with columnar grain structure. The samples loaded in the transverse direction reveal regions of brittle grain boundary fracture, distinct vertical columnar grains parallel to the fracture surface, and regions of ductile shear. Like Figure 8, the fracture initiates on the grain boundaries by the linkage of voids that cause total grain boundary separation. The grains maintain integrity along the long axis even with grain boundary failure between columnar grains. As the quantity of material remaining to resist the applied load is reduced, the internal stress increases enough for the remaining material to neck, causing the ductile shear. This result shows the benefit of reducing transverse grain boundaries. Again, the creep curves show a short tertiary regime, less than 400 hours. This confirms the brittle nature of the fracture of the transverse loaded samples, with minimal reduction in cross-sectional area, and regions of cleavage facets. Kuo *et al.*<sup>[28]</sup> also observed such features, where the authors demonstrated that cracking was initiated along transverse dendrites and grain boundaries where  $\delta$ -phase was present. However, the current samples with columnar grain structure and loaded in the longitudinal direction show a cup/cone ductile failure. The ductile nature of the samples in the longitudinal direction is observed in the creep curve, where the tertiary regime is greater than 1000 hours.

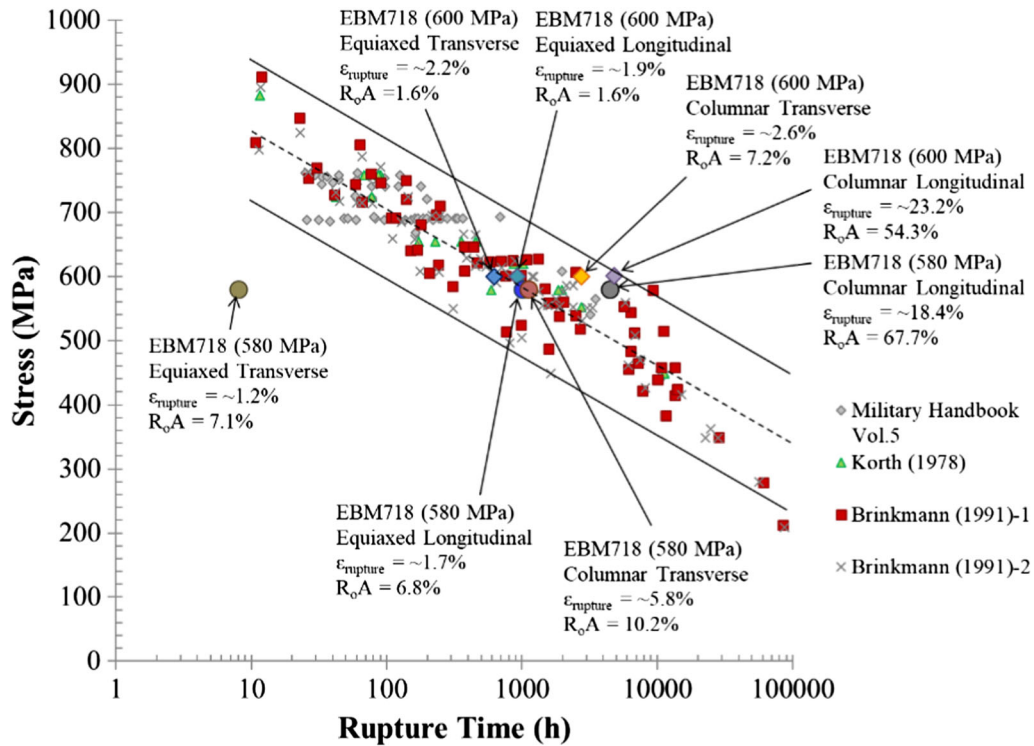


Fig. 5—Relationship between applied stress and rupture time comparing creep properties of EBM Inconel 718 with conventional material. Note the spread in the creep life of conventional material and the good agreement with EBM Inconel 718.

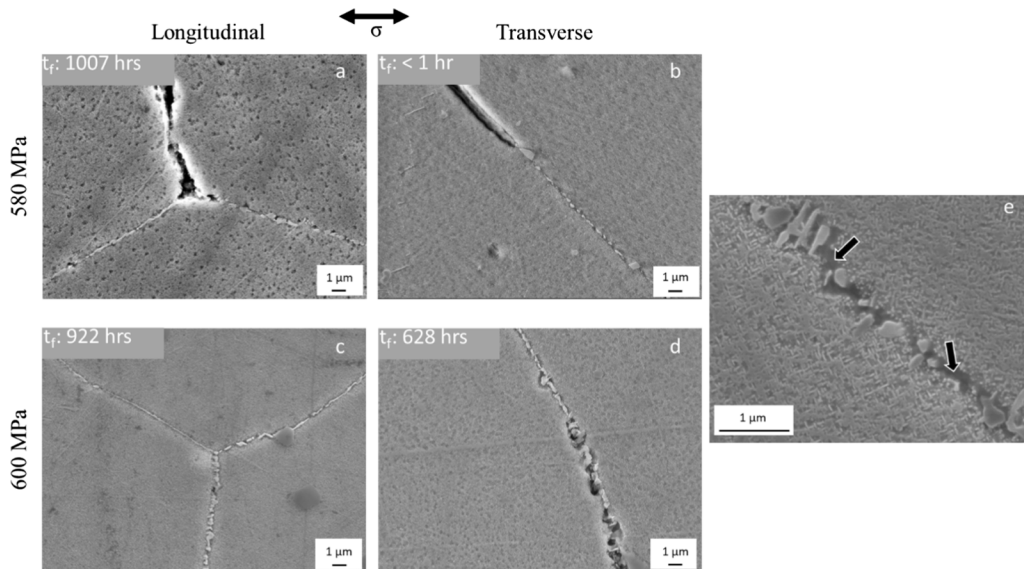


Fig. 6—SEM images of point net melt strategy (equiaxed grain structure), showing creep crack voids forming along the  $\delta$ -rich grain boundaries. Precipitate-free zones close to grain boundaries are observed. Creep conditions: 923 K (650 °C) stress and loading direction orientated to build direction are labeled. (a, c) are samples in the longitudinal direction loaded at 580 and 600 MPa, respectively. (b, d) are samples in the transverse direction loaded at 580 and 600 MPa, respectively. (e) is a high-magnification image of Figure 6(a), the PFZ is shown with black arrows.

#### IV. DISCUSSION

At high temperatures, there is a dependence of applied stress on the steady-state or minimum creep rate for metals and alloys. The relationship can be approximately evaluated using the Norton relationship,<sup>[31]</sup>

described by  $\dot{\epsilon}_{\min} = A'\sigma^n$ , where  $A'$  is a material constant,  $n$  is the stress exponent,  $\dot{\epsilon}_{\min}$  is the minimum strain rate, and  $\sigma$  is the applied stress. For simple alloys, the value of the stress exponent ( $n$ ) is equal to or less than 5, while for systems strengthened by second phases, like

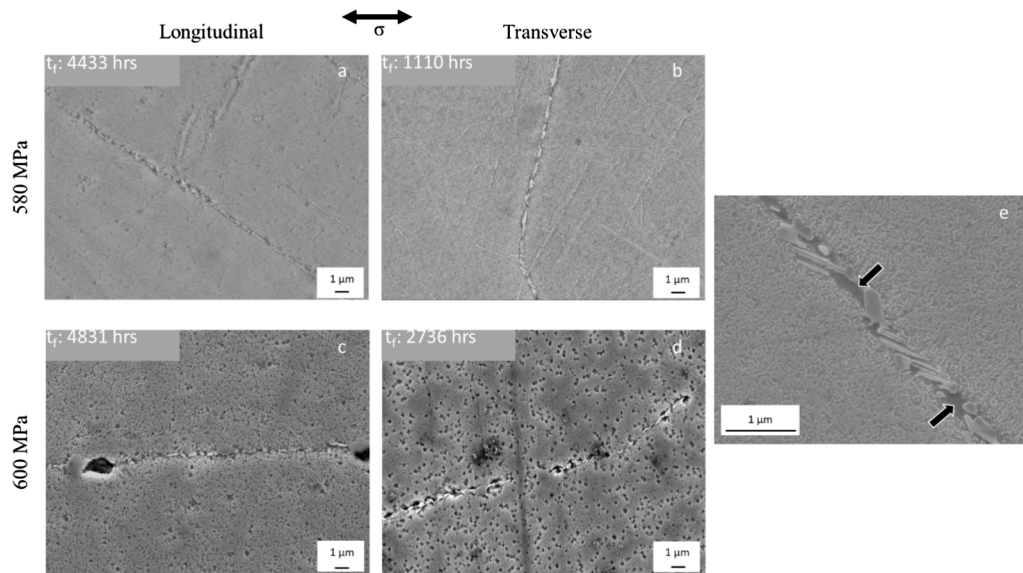


Fig. 7—SEM images of standard melt strategy (columnar grain structure), showing creep crack voids forming along the  $\delta$ -rich grain boundaries. Precipitate-free zones close to grain boundaries are observed. Creep conditions: 923 K (650 °C), stress and loading direction orientated to build direction are labeled. (a, c) are samples in the longitudinal direction loaded at 580 and 600 MPa, respectively. (b, d) are samples in the transverse direction loaded at 580 and 600 MPa, respectively. (e) is a high-magnification image of Figure 7(a), the PFZ is shown with black arrows.

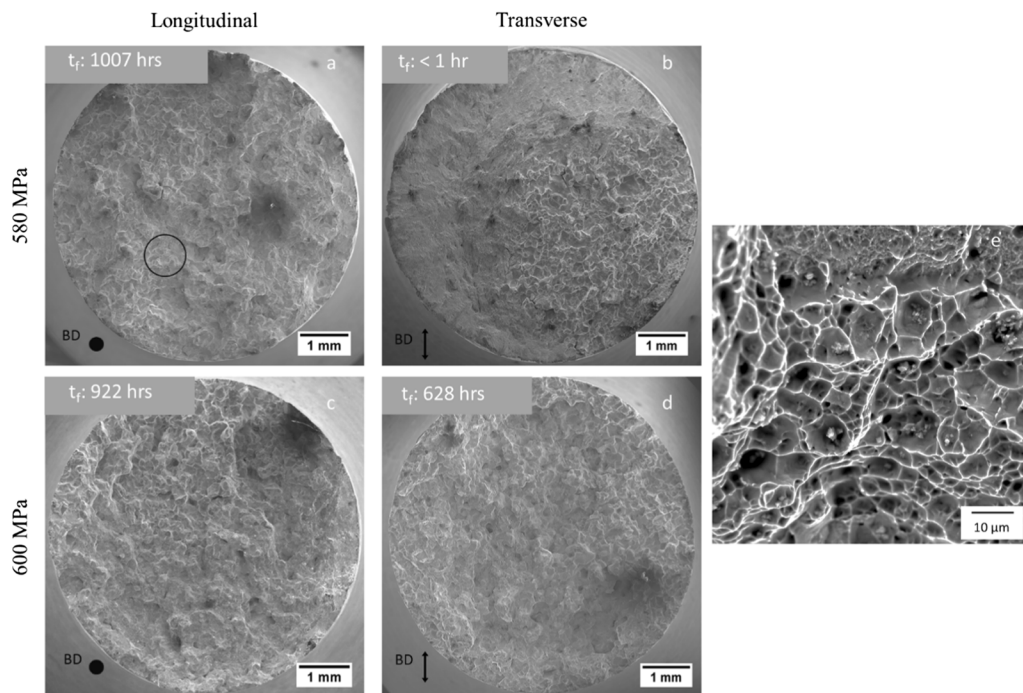


Fig. 8—Fractography of point net melt strategy (equiaxed grain structure). Grain boundary cleavage is evident. This illustrates grain boundary failure. The short failure times show the effect of increase transverse grain boundary area. Creep conditions: 923 K (650 °C), build direction are labeled. (a, c) are samples in the longitudinal direction loaded at 580 and 600 MPa, respectively. (b, d) are samples in the transverse direction loaded at 580 and 600 MPa, respectively. (e) is a high-magnification image from the black circle in Fig. 8(a), particles can be seen at the bottom of the cups where creep voids accumulated.

Inconel 718, higher values of  $n$  are observed.<sup>[20,32–34]</sup> The value of  $n$  corresponds to a creep deformation mechanism. For  $n$  values 5 or greater, dislocation creep is the rate-limiting deformation mechanism. Inconel 718, in

particular, has  $n$  values of 14–18.<sup>[20,26]</sup> Figure 10 shows the stress dependence of the steady-state creep rate at 923 K (650 °C) for conventionally processed Inconel 718 plotted with the current results.<sup>[17,20,26]</sup> The EBM



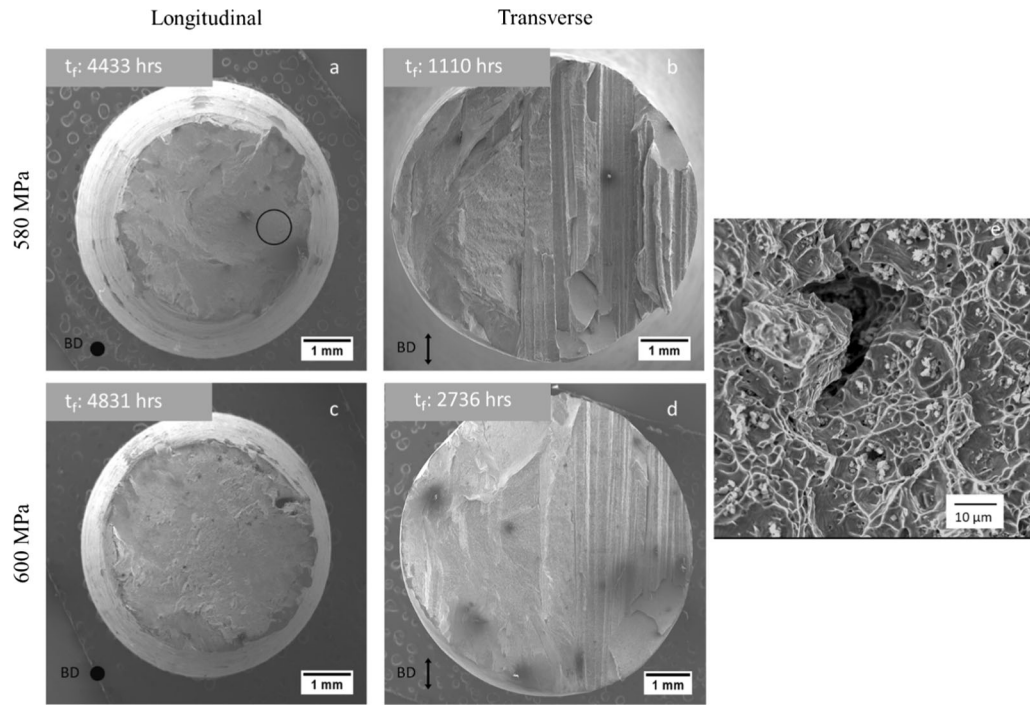


Fig. 9—Fractography of standard melt strategy (Columnar grain structure). Grain boundary cleavage is evident. This illustrates grain boundary failure. The short failure times show the effect of increase transverse grain boundary area. Creep conditions: 923 K (650 °C), build direction are labeled. (a, c) are samples in the longitudinal direction loaded at 580 and 600 MPa, respectively. (b, d) are samples in the transverse direction loaded at 580 and 600 MPa, respectively. (e) is a high-magnification image from the black circle in Fig. 9(a), particles can be seen at the bottom of the cups where creep voids accumulated.

Inconel 718 samples show a good agreement with literature data; thus, it can be concluded that the mechanism is dominated by dislocation creep.

The microstructure correlates the creep deformation mechanism to the creep performance, by controlling dislocation motion, grain boundary motion, or damage accumulation rate. Since the deformation mechanism has been established as dislocation creep, the grain size does not play a large role in creep rate.<sup>[35]</sup> However, the precipitate distribution, grain boundary precipitates, and orientation of grain boundaries with respect to the direction of tensile load do play a dominant role. Figures 6 and 7 show the microstructure after creep rupture. The matrix contains a dispersion of fine  $\gamma'$  and  $\gamma''$ , (20 to 40 nm), with a small interparticle spacing. The particle distribution causes a back or threshold stress, which can be modeled using  $\dot{\epsilon}_{\min} = A'(\sigma_o - \sigma_{th})^n$ , where  $\sigma_o$  is the applied stress and  $\sigma_{th}$  is the threshold stress.<sup>[36–38]</sup> The threshold stress restricts dislocation motion. This restriction gives Inconel 718 its superior creep rate at high temperature and stresses. However, grain boundaries are a point of weakness in metals, as they are sinks for defects, in particular, grain boundaries transverse to the tensile load direction.<sup>[39–44]</sup> The number of precipitates on the grain boundaries affects the damage accumulation rate, which in turn affects the time to failure. Chen *et al.*<sup>[19,45]</sup> showed that the shape of the creep rate versus time curves varies with the amount of the  $\delta$  precipitates in the grain boundaries. At 795 MPa and 898 K (625 °C), there seemed to be a significant

duration in the steady-state creep stage if the grain boundaries had a lineal density of at least 61 pct precipitates. The authors also observed the formation of small isolated creep voids around  $\delta$  precipitates along grain boundaries towards the end of the steady-state stage, leading into the tertiary stage.

With the aging of  $\delta$  precipitates on the grain boundaries, a PFZ can form. The presence of a PFZ can accelerate creep damage. As described in section 4.3, the PFZ can form from the dissociation of  $\gamma''$  by the coarsening and formation of  $\delta$  phase. The PFZ consists only of the soft  $\gamma$  matrix. The soft matrix accommodates stresses by allowing dislocation mobility and pile up which initiates crack formation. The creep damage in the PFZ along the  $\gamma/\delta$  boundary can be seen as voids. Creep fracture then initiates along the  $\delta$ -rich transverse grain boundaries. All the test specimens exhibit intergranular cracking originating from  $\delta$ -induced voids. Shassere *et al.*<sup>[46]</sup> showed evidence of deformation in a PFZ of an Fe-Cr-Al alloy strengthened by  $Fe_2Nb$  Laves phase. Electron backscatter diffraction was used to observe crystal rotation in the PFZ; this was attributed to mobile dislocations. The authors proposed that there is a relationship between the width of the PFZ and the fraction of particles on the grain boundary. Both Chen *et al.*<sup>[19,45]</sup> and Shassere *et al.*<sup>[46]</sup> showed that grain boundary precipitates and the presence of a PFZ play an important role in creep deformation of multiphase materials, where the failure mechanisms are confined to the grain boundary regions, even if the creep deformation mechanism is dislocation dominant. In the

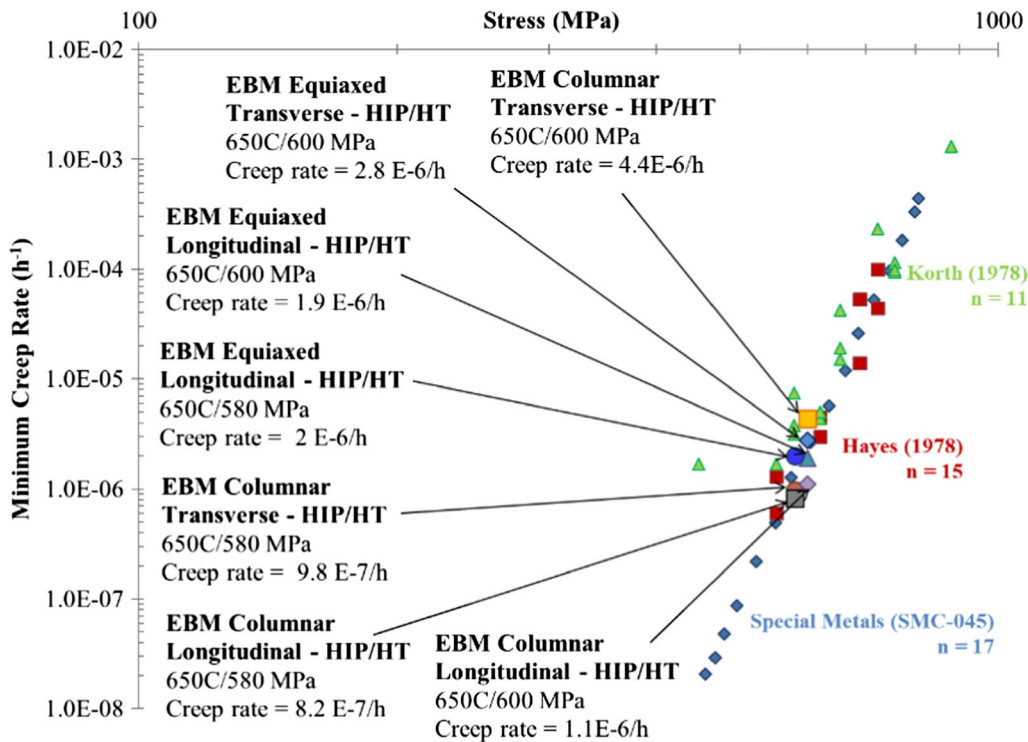


Fig. 10—Stress dependence of the steady-state creep rate of EBM Inconel 718 investigated in this work compared with conventional material.

current work, both builds with equiaxed grain structure or columnar grains, loaded transversely, revealed the transverse grain boundaries were preferential sites for damage to accumulate and cause creep rupture faster than samples with columnar grains loaded longitudinally. The results presented demonstrate the importance of reducing transverse grain boundaries in creep deformation of AM Inconel 718. However, a benefit of AM EBM is that the microstructures can be tailored locally, to allow both tensile and fatigue mechanical strength from an equiaxed microstructure and high-temperature creep resistance from a columnar microstructure.

## V. CONCLUSIONS

In this work, the effect of texture on creep deformation of EBM Inconel 718 has been demonstrated. The similar creep lifetimes obtained for the EBM materials compared to the conventionally processed material indicate the feasibility of EBM to produce Inconel 718 components needed for the high-temperature industrial applications. The properties of Inconel 718 agree with longstanding observations that columnar materials with grains oriented parallel to the stress axis have superior creep properties. The role of the  $\delta$  phase in the creep rupture ductility is equivalent in both EBM Inconel 718 and conventionally processed material. The combination of EBM and post-processing conditions used in the current investigation gives beneficial creep properties. Although EBM of Inconel 718 is not universally suited for generic application, microstructures can be tailored

to the type of service load and optimized to produce multi-grain structured components.

The results of the current work show comparable creep rupture properties to conventional wrought Inconel 718. A summary of the results is listed below:

1. Two different melt strategies were used to produce two different grain morphologies. Both equiaxed and columnar grains were produced and maintained after post-processing.
2. Before creep testing, the microstructures in all samples contained a  $\gamma$  matrix with  $\gamma'/\gamma''$  precipitates. The grain boundaries contained carbides and  $\delta$  phase.
3. The creep samples with equiaxed microstructures had the shortest time to rupture (< 1000 hours), and the samples with columnar microstructures, loaded in the longitudinal direction, had the longest time to failure (approximately 4500 hours). All the creep times to rupture, excluded the anomalous sample, fall within the scatter band of wrought Inconel 718 at 923 K (650 °C), demonstrating the HIPed EBM Inconel 718 is comparable to wrought product.
4. Voids and cracking were observed on grain boundaries in all the creep rupture samples, except for the columnar longitudinal sample which only contained voids. The grain boundaries transverse to the tensile load contained the maximum number of voids and cracks. A small PFZ was observed, in all samples, around the grain boundary  $\delta$  phase.
5. Fractography revealed grain boundary cleavage in the samples with equiaxed microstructures. A mixture of grain boundary cleavage and ductile shear was observed in the columnar transverse loaded

samples. Only ductile failure was observed in columnar longitudinally loaded samples. This indicates transverse grain boundaries are detrimental to overall creep rupture properties of EBM Inconel 718.

6. In agreement with existing literature, the creep deformation mechanism was dislocation creep. The importance of grain boundary precipitates and the presence of a PFZ allowed the accumulation of creep damage that in turn affected rupture.

## ACKNOWLEDGMENTS

The authors thank Dr. Frederick List and Thomas Muth at Oak Ridge National Laboratory for their comments on this manuscript. The authors also thank Jeremy Moser for helping in conducting creep tests and Andres Rossy for obtaining the EBSD images. Further, the authors would like to acknowledge Dr. Anders Eklund at Qunitus Technologies for his help in providing the hot isostatic press capability to post-process the material used in this work. This research is sponsored by the US Department of Energy, Office of Energy Efficiency and Renewable Energy, Advanced Manufacturing Office, under Contract DE-AC05-00OR22725 with UT-Battelle, LLC.

## REFERENCES

1. R.C. Reed: *The Superalloys: Fundamentals and Applications*, Cambridge University Press, Cambridge, 2006.
2. H.J. Wagner and A.M. Hall: Physical metallurgy of alloy 718, No. DMIC-217, Defense Metals Information Center, Battelle Memorial Institute, Columbus, OH, 1965.
3. A. Lingenfelter: *Superalloy*, 1989, vol. 718, pp. 673–83.
4. J.F. Radavich: in *Conference Proceedings on Superalloy*, 1989, pp. 229–40.
5. K. Sano, N. Oono, S. Ukai, S. Hayashi, T. Inoue, S. Yamashita, and T. Yoshitake: *J. Nucl. Mater.*, 2013, vol. 442, pp. 389–93.
6. M. Burke and M. Miller: ed. *EA Loria, Minerals, Met. And Mat. Society*, 1991, pp. 447–56.
7. S. Li, J. Zhuang, J. Yang, and X. Xie: *Superalloys*, 1994, vol. 718, pp. 625–706.
8. S. Azadian, L.-Y. Wei, and R. Warren: *Mater. Charact.*, 2004, vol. 53, pp. 7–16.
9. M. Anderson, A.L. Thielin, F. Bridier, P. Bocher, and J. Savoie: *Mater. Sci. Eng. A*, 2017, vol. 679, pp. 48–55.
10. I. Gibson, D.W. Rosen, and B. Stucker: *Additive Manufacturing Technologies*, Springer, Berlin, 2010, pp. 299–32.
11. K.N. Amato, S.M. Gaytan, L.E. Murr, E. Martinez, P.W. Shindo, J. Hernandez, S. Collins, and F. Medina: *Acta Mater.*, 2012, vol. 60, pp. 2229–39.
12. W.J. Sames, K.A. Unocic, R.R. Dehoff, T. Lolla, and S.S. Babu: *J. Mater. Res.*, 2014, vol. 29, pp. 1920–30.
13. Y. Tian, D. McAllister, H. Colijn, M. Mills, D. Farson, M. Nordin, and S. Babu: *Metall. Mater. Trans. A*, 2014, vol. 45, pp. 4470–83.
14. M. Kirka, K. Unocic, N. Raghavan, F. Medina, R. Dehoff, and S. Babu: *JOM*, 2016, vol. 68, pp. 1012–20.
15. M.M. Kirka, F. Medina, R. Dehoff, and A. Okello: *Mater. Sci. Eng. A*, 2017, vol. 680, pp. 338–46.
16. M.M. Kirka, Y. Lee, D.A. Greeley, A. Okello, M.J. Goin, M.T. Pearce, and R.R. Dehoff: *JOM*, 2017, vol. 69, pp. 523–31.
17. *Special Metals: Special Metals Corporation*, 2007, 045, pp. 1–28.
18. ASTM-E139-11: *ASTM International*, 2011.
19. W. Chen and M. Chaturvedi: *Mater. Sci. Eng. A*, 1994, vol. 183, pp. 81–89.
20. R. Hayes: *Superalloys 718, 625 and Various Derivatives*, 549–61.
21. F. VerSnyder and R. Guard: *Trans. ASM*, 1960, vol. 52, p. 485.
22. G. Edward and M.F. Ashby: *Acta Metall. Mater.*, 1979, vol. 27, pp. 1505–18.
23. T. Lillo, J. Cole, M. Frary, and S. Schlegel: *Metall. Mater. Trans. A*, 2009, vol. 40, p. 2803.
24. B. Kear and B. Pearcey: *AIME Trans.*, 1967, vol. 239, pp. 1209–15.
25. C. Brinkman, M. Booker, and J. Ding: *Superalloys*, 1991, vol. 718, pp. 519–36.
26. G. Korth and G. Smolik, Idaho National Engineering Lab., Idaho Falls (USA), 1978.
27. Department-of-Defense: *Military Handbook*, 1998, 5, 1–1653.
28. Y.-L. Kuo, S. Horikawa, and K. Kakehi: *Scr. Mater.*, 2017, vol. 129, pp. 74–78.
29. S. Antolovich: in *Proceedings of the International Symposium on the Metallurgy and Applications of Superalloy 718*, 1989, pp. 647–53.
30. G.A. Rao, M. Kumar, M. Srinivas, and D. Sarma: *Mater. Sci. Eng. A*, 2003, vol. 355, pp. 114–25.
31. F.H. Norton: *The Creep of Steel at High Temperatures*, McGraw-Hill Book Company, Incorporated, 1929.
32. H. Burt and B. Wilshire: *Metall. Mater. Trans. A*, 2004, vol. 35, p. 1691.
33. S. Spigarelli, E. Cerri, P. Bianchi, and E. Evangelista: *Mater. Sci. Tech.*, 1999, vol. 15, pp. 1433–40.
34. T. Shrestha, M. Basirat, I. Charit, G.P. Potirniche, K.K. Rink, and U. Sahaym: *J. Nucl. Mater.*, 2012, vol. 423, pp. 110–19.
35. T.G. Langdon and F.A. Mohamed: *J. Mater. Sci.*, 1978, vol. 13, pp. 1282–90.
36. J. Čadek: *Mater. Sci. Eng.*, 1987, vol. 94, pp. 79–92.
37. Y. Han and M. Chaturvedi: *Mater. Sci. Eng.*, 1987, vol. 85, pp. 59–65.
38. B.A. Shassere, Y. Yamamoto, and S.S. Babu: *Metall. Mater. Trans. A*, 2016, vol. 47, pp. 2188–2200.
39. B. Burton: *Mater. Sci. Eng.*, 1973, vol. 11, p. 337.
40. G.L. Dunlop, J.O. Nilsson, and P.R. Howell: *J. Microsc.-Oxford*, 1979, vol. 116, pp. 115–22.
41. J. Harris: *Metal. Sci. J.*, 1973, vol. 7, pp. 1–6.
42. F.A. Mohamed and T.G. Langdon: *Acta Metall. Mater.*, 1974, vol. 22, pp. 779–88.
43. A.J. Perry: *J. Mater. Sci.*, 1974, vol. 9, pp. 1016–39.
44. J. Wadsworth, O.A. Ruano, and O.D. Sherby: *Metall. Mater. Trans. A*, 2002, vol. 33, pp. 219–29.
45. W. Chen and M. Chaturvedi: *Acta Mater.*, 1997, vol. 45, pp. 2735–46.
46. B. Shassere, Y. Yamamoto, J. Poplawsky, W. Guo, and S.S. Babu: *Metall. Mater. Trans. A*, 2017, vol. 48, pp. 4598–14.